Multicomponent Synergistic Contribution in Nanoengineered Nanofibers for Flexible Energy Storage

Original
Multicomponent Synergistic Contribution in Nanoengineered Nanofibers for Flexible Energy Storage / Boll, Felix; Fadda, Marta; Happel, Melissa; Crisci, Matteo; Athanassiou, Athanassia; Smarsly, Bernd; Bella, Federico; Lamberti, Francesco; Perotto, Giovanni; Gatti, Teresa. - In: ACS APPLIED ENERGY MATERIALS. - ISSN 2574-0962. - 7:11(2024), pp. 4733-4744. [10.1021/acsaem.4c00417]

Publisher:
ACS

Published
DOI:10.1021/acsaem.4c00417

Multicomponent synergistic contribution in nano-engineered nano-fibers for flexible energy storage

Felix Boll,[1,2] Marta Fadda,[3] Melissa Happel,[1,2] Matteo Crisci,[1,2] Athanassia Athanassiou,[3] Bernd Smarsly,[1,2] Federico Bella,[4] Francesco Lamberti,[5] Giovanni Perotto,[3] Teresa Gatti[1,2,4*]

[1] Institute of Physical Chemistry, Justus Liebig University, Heinrich-Buff-Ring 17, 35392 Giessen, Germany

[2] Center for Materials Research, Justus Liebig University, Heinrich-Buff-Ring 17, 35392 Giessen, Germany

[3] Smart Materials, Istituto Italiano di Tecnologia, via Morego 30, 16163 Genoa, Italy

[4] Department of Applied Science and Technology, Politecnico di Torino, Corso Duca degli Abruzzi, 10129 Turin, Italy

[5] Department of Chemical Sciences, University of Padova, via Marzolo 1, 35131 Padova, Italy

* E-mail: teresa.gatti@polito.it

Abstract

Lightweight and flexible energy storage devices are gaining interest due to their potential integration into wearable electronics. They might work for the long-term powering of sensors, for example, but they need to be operative after application of different types of mechanical stress. Conductive and semiconducting nanomaterials are largely investigated as active components for this type of application but need to be coupled to an elastic matrix, such as a polymeric one, in order to be functional in flexible technologies. In this work, we investigate the production of electrospun nanofibers based on a ternary blend of 2D layered WS_2, multi-walled carbon nanotubes and carbon black in polyethylene oxide and characterize their electrochemical behaviour in symmetric supercapacitor architectures within bendable pouch cells, in conjunction with a robust analysis of the active materials' mechanical properties. We find optimized specific capacitance values of up to 9 F g^{-1} after mechanical adjustment of the device and excellent capacitance retention after multiple bending cycles, revealing the potential of similar scaffolds for use in wearable energy storage devices to activate low-power electronics.

Keywords

Polymer nanofibers, nanocomposite, electrospinning, energy storage, flexible device

1. Introduction

With the emergence of a continuously increasing request of smart electronic devices in portable and wearable shapes, also the demand for flexible power sources is outpacing, to prevent any limitation in terms of functionality and design.[1] Especially for sensors and applications in the health sector, biocompatible, lightweight, and non-hazardous power sources are of interest to ensure safety.[2,3] However, for running stretchable sensors and devices, the storage of electrical energy is considered to be the current bottleneck to allow the effective commercialization of these technologies. Since many sensors are already well functioning and largely available, their powering over long-term is considered a major issue.[4,5] In this context, several eco-friendly and flexible supercapacitors and triboelectric generators have been reported in the last years as successful examples of energy devices with potential for future application as power units for wearable and lightweight electronics.[6–8]

Mainly carbon-based materials are used for the fabrication of electrochemical double layer capacitors (EDLCs). Long-term cycle stability and fast charge/discharge behaviour are exceptional arguments in favour of the usage of these devices. Also, differing shapes for the active layer can be adopted, from fibres to membranes, depending on the specific need.[9–11] Carbon-based species, especially carbon nanotubes and graphene-based materials, are interesting for these scope due to the excellent electrical conductivity and good mechanical resistance, with, for instance, Young's moduli of up to 950 GPa for multi walled carbon nanotubes (MWCNTs).[12] Unfortunately, stacking, aggregation and entanglement in these nanomaterials can drastically decrease their theoretical capacitive performance.[13] To further push the specific capacitance (C_s) of nanocarbons, their combination with transition metal dichalcogenides (TMDs) could be a valuable strategy to pursue. Especially, WS_2 emerges for its performance, with a large C_s of about 1439.5 F g^{-1} reported in a three-electrode setup at 5 mA cm^{-2} in a 3 M KOH electrolyte medium.[14] In general, many works on TMD-based materials in their layered (2D) form, as well as in both their semiconducting and metallic phases, can be found in the literature, in which they are often combined with carbon-based backbones like carbon cloth, carbon nanofibers (CNFs) and other carbon materials.[15–20]

However, CNFs for instance, are mainly produced from polyacrylonitrile or polyvinyl pyrrolidone, where toxic solvents like N,N-dimethylformamide and tetrahydrofuran have to be used for preparation. Furthermore, large temperatures up to 900 °C under reducing atmosphere are commonly used to produce them.[21,22] Also for exfoliation of TMDs, toxic solvents are generally used, being N-methylpyrrolidone the most prominent example.[23–25] However, also non-toxic solvents can be employed for both fibers production and for the exfoliation of TMDs. To adhere as much as possible to green methods, ethanol, isopropanol (IPA) and water are good choices of liquid media for processing.[26]

Polyethylene oxide (PEO) is the most common polymer source for producing nanofibers with the above described solvents.[27,28] Since PEO is a highly insulating polymer, conductive carbon sources like MWCNTs and carbon black (CB) produced from recycled tires were used in this study to significantly increase the electrical conductivity in polymeric nanofibers obtained by electrospinning.[29] For PEO films mixed with MWCNTs, the conductivity was reported to increase by seven orders of magnitude.[30] A similar strong increase (almost twelve orders of magnitude) was obtained for PEO-MWCNTs electrospun fibers, at 1 wt% of MWCNTs.[31] The percolation threshold is greatly dependent on the aspect ratio of the MWCNTs and therefore mainly influenced by the degree of dissolution in the solvent preventing aggregation.[31–33] Inks of 2D-WS_2 can be sustainably produced through a top-down approach using surfactant-assisted liquid phase exfoliation (SA-LPE), in a mixture of IPA and water.[34] By using SA-LPE with non-toxic solvents, expensive and toxic precursor materials can be avoided, while no large and expensive equipment has to be used, as it is the case for bottom-up methods like chemical vapor deposition and atomic layer deposition.[35]

In this work, we report on composite nanofibers based on PEO filled with 2D-WS_2, MWCNTs, and CB, where mass ratios were tuned to enable good electrical conductivity and capability of storing charges, through a synergistic contribution of all the three involved components, which does not take place in simpler mixtures like the mono-filler or binary ones.[36,37] By resorting to the use of low-cost methods and green solvents like IPA and water, as well as abundant and recycled materials, we propose a novel platform for capacitive energy storage, with the added value of featuring good flexibility for incorporation into wearable technologies. These nano-engineered items show a notable resilience against mechanical stress and we demonstrate this by investigating the influence of repetitive bending on the charge-storage ability in symmetric capacitor architectures. All these characteristics are important for enabling the development of flexible EDLCs for smart and wearable devices.

2. Experimental Section

2.1 Materials and methods

All solvents and chemicals were purchased from Sigma-Aldrich and used directly without further purification unless otherwise specified. Two-dimensional WS_2 particles were produced following an already established protocol elaborated and described in a former publication by some of us, based on SA-LPE method.[34] The supernatant obtained from this method is filtered using a polytetrafluoroethylene (PTFE) filter with a pore size of 200 µm utilizing a filter setup, as shown in the Supporting Information (S.I.). The 2D-WS_2 particles are then re-dispersed in a mixture of IPA and water in a 7:3 (70 %v/v IPA, 30 %v/v H_2O) ratio using an ultrasonic bath (USB) for 10 min at a frequency of 37 kHz. The concentrated suspension is placed into a drying furnace at 120 °C for 12 h to evaporate both solvents. The residual powder is scratched out of the vessel and can be used after re-dissolution in aqueous solutions with a precise weight ratio. As shown in the S.I., it can be proved by Raman measurements that the mono- and few-layered composition of the exfoliated sample is retained even after the filtration and re-dispersion procedures. The suspension of MWCNTs was produced by dissolving PEO with an average molecular weight of 1.000.000 g mol^{-1} at a concentration of 0.5 mg mL^{-1} into a mixture of IPA and H_2O in a 7:3 ratio. Carboxylic acid-functionalized MWCNTs were addS1ed into the solution, at a concentration of 0.5 mg mL^{-1}. For producing a homogenous suspension of functionalized MWCNTs, a tip sonicator Sonoplus HD 2200 from Bandelin Electronic was utilized, as shown in the S.I.

Scanning electron microscopy (SEM) images were collected on a Gemini SEM 560 from Zeiss with an acceleration voltage of 3 kV and an aperture size of 20.0 µm. The images were collected with the secondary electron detector. Energy-dispersive X-ray spectroscopy (EDS) measurements were performed using an Ultimax detector from Oxford Instruments with an acceleration voltage of 5 kV and an aperture size of 75.0 µm. Samples were observed also through scanning transmission electron microscopy (STEM) with a non-aberration corrected microscope (Talos F200X, ThermoScientific) operated at 200 kV. Images were recorded on a 16Mpxls CMOS camera with a 1 s exposure time. STEM images and EDS maps were acquired with the same microscope operated in STEM mode with a probe current of 750 pA. EDS spectra were acquired with an in-column 4-quadrant detector. Elemental maps were elaborated from the machine acquisition software (Velox, V. 3.6.0). Raman spectra were recorded with a Senterra infinity 1 from Bruker in a range from 200 – 1700 cm^{-1}, with an optical microscope for adjusting and a magnification factor of 50. The excitation laser was operating at a wavelength of 532 nm. X-ray diffraction (XRD) data were obtained with a X'Pert Pro MRD from Malvern Panalytical. A Cu K_α source ($\lambda = 0.154178$ nm) was used at a voltage of 40 kV and a current of 40 mA. The incident beam angle was set to 0.5°, with a 2 mm mask and a cover slit of 1/16 °. Samples were measured in the 2θ range of 10–80°. Thermogravimetric analysis (TGA) coupled with mass spectrometry were carried out in synthetic air (79 vol.% N_2 and 21 vol.% O_2) using a STA40PC thermoscale provided by Netzsch within a temperature ranging from 30 until 700 °C with a heating ramp of 2 K min^{-1}.

The mechanical properties of nanofibrous composites were evaluated by uniaxial tension tests using a dual-column universal testing machine Instron 3365 (Instron, Norwood, MA, USA). Since fiber mats are very fragile and thin, they could not be cut in the typical dog bone shape. To perform the measurement, firstly, fiber mats were cut in specimens with a width of 4 mm and length of 25 mm, and then placed in a paper frame as support. At least 10 samples for each type were tested in order to improve the reliability of the results. Before the test, all the samples were conditioned at 24 °C and 50% relative humidity. in an Espec SH-262 Environmental Chamber (ESPEC, Hudsonville, MI, USA). Displacement was applied at a rate of 10 mm min^{-1}. The Young's modulus (YM), ultimate tensile strength (UTS), and elongation at break (EB) were reported. Electrochemical characterization was performed with the Autolab PGSTAT302 from Metrohm and the Nova Software (version 2.1). Cyclic voltammograms were recorded in the range from -0.25 – 0.6 V with scan steps of 2.44 mV at different scan rates of 10 mV s^{-1}, 20 mV s^{-1}, 50 mV s^{-1}, 100 mV s^{-1}, 150 mV s^{-1}, 200 mV s^{-1}, 250 mV s^{-1}, and 500 mV s^{-1}. The cycling was done 6 times to ensure the equilibrium state of samples and only the polygon area of the last cycle was used for calculating the specific capacitance using the polygon area function of OriginPro (2021). The measurements were the same for all types of cells (Swagelok and pouch cells). Potentiostatic electrochemical impedance spectroscopy (PEIS) measurements were done using the galvanostatic potentiostat BioLogic from the frequency range of 0.1 Hz up to 100.000 Hz in combination with a Swagelok electrochemical cell.

2.2 Blend preparation and electrospinning

The as-prepared precursor materials were employed for the preparation of blends for the electrospinning process. As liquid basis, the 0.5 mg mL^{-1} concentrated MWCNTs suspension was mixed with a CB produced from recycled tires, the synthesis of which was already reported by some of us,[29] with a mass ratio of 0.1 wt%, namely a concentration of 1 mg mL^{-1}.The mixture was homogenized using an USB at a frequency of 37 kHz for 30 min to ensure the proper mixing of the CB (see S.I.). Subsequently, exfoliated 2D-WS_2 was added under stirring for 30 min, with a mass ratio of 1.25 wt%. The USB was again used for homogenisation at 37 kHz and 30 min. The fourth and last additive, PEO (M_w = 1.000.000 g mol^{-1}), was added to the suspension with a mass ratio of 2.5 wt%. The mixture containing MWCNTs, CB, 2D-WS_2, and PEO was stirred and mixed for another 2 h to ensure the complete dissolution of PEO. Afterwards, the suspension was added to a planetary ball mill at a rotation speed of 250 revolutions per minute (rpm) for 3 h to further homogenize and finally produce the blends, by decreasing the size of all dissolved or suspended species (depicted in the S.I.). The particle size is essential for the electrospinning process since the tip of the syringe easily gets clogged using non-ideal, heterogeneous suspensions. Furthermore, a continuous flow of the blend must be ensured, since the production of fibers necessarily demands a stable Taylor cone to get reproducible appearances and diameters and to avoid electro-spraying. After another 12 h of stirring, the blend was ready to be spun in the electrospinning setup. A potential of –2 kV was applied to a rotating drum roll as fiber collector, which was covered with aluminium foil (for easy and clean removal), where the rotation enables a more homogeneous production of fibers compared to a static current collector. A syringe tip was used as a counter electrode at a distance of 25 cm apart from the drum roll and an applied potential of 14 kV was used while electrospinning. For the processing, the blend was put into a syringe with the before mentioned syringe tip, having a diameter of 0.5 mm. Finally, a constant flow rate of 0.3 mL h^{-1} was set and the drum collector rotated at 60 rpm.

2.3 Fabrication of pouch cells

For the preparation of pouch cells, a flexible CB-PTFE current collector (CB-PTFE CC) was produced using a commercially available CB (Beyond Battery, Singapore) and PTFE. An aqueous PTFE dispersion (60 wt%) containing traces of polyethylene glycol trimethyl nonyl ether was mixed with 2 mL ethanol and with the CB. The ratio between CB and PTFE was set to 95:5 wt%. The suspension was stirred to successively evaporate ethanol. Once a rubbery consistency was achieved, ethanol was added dropwise to the mixture and kneaded into the clump using a spatula. After 10-15 min during which the mixture was homogenized, a glass plate and glass rod were used to roll a sheet with a thickness in the range of 70-100 µm. The as-prepared sheets were dried over night at 80 °C. Placed on the current collector while electrospinning, fibrous materials can be directly deposited onto the CB-PTFE CC (see in S.I.). After preparation of the current collector-fiber composites, the stacked material was punched into coin-shaped pieces with diameters of 12 mm and 14 mm to produce flexible pouch cell devices. The different diameters ensure total area overlapping, so that direct charge transfer is guaranteed. A round SiO_2 nanofiber piece with a diameter of 17 mm was used as a separator. The pouch cells were assembled using 140 µL of 1 M tetra ethylammonium tetrafluoroborate ($TEABF_4$) in propylene carbonate (PC) as electrolyte. Nickel tabs were used as contacts for both sides of the pouch cell since a symmetric device was produced. Finally, the cells were closed under vacuum using pouch cell bags and a sealing device (Sealervac) from Sealershop, with an evacuation time of 60 s and a sealing time of 5 s.

2.4 Electrochemical testing

Two different cell types were used for electrochemical characterization. First, a symmetric supercapacitor device was built in a typical Swagelok cell type, as shown in the SI. Two pieces of composite fibers of 12 mm in diameter were separated by a Whatman SiO_2 nanofiber sheet (14 mm). All components, different to the pouch cells, were contacted with 120 μL of electrolyte, i.e. a 0.5 M $TEABF_4$ solution in PC. Finally, the Swagelok cell was pressurized by springs, closed, and contacted for measuring. The second cell type was the as-prepared pouch cells, the fabrication of which is described above. The cells were directly connected to a potentiostat using crocodile clamps. Mainly, we used electrochemical cyclic voltammetry data (CV) to elaborate the C_s of the produced ternary nanofibers (see S.I.). The measurements were done at a constant temperature of about 23 °C. The potential window has been set between -0.25 V and 0.6 V, which is the maximum range of the non-Faradic region. For referencing CV data, a 0.5 M $TEABF_4$ solution in PC was mixed with ferrocene to enable comparability to other electrochemical systems. In the ascribed region, no redox processes are responsible for charge accumulation, but surface charging.[38–40] Different scan rates were used from 10 mV s^{-1} up to 500 mV s^{-1} (see above).

3. Results and Discussion

The different steps for the blend preparation described under 2.1 and 2.2 are summarized in **Figure S1**. From these blends, nanofibers are produced by using electrospinning, as sketched in **Figure 1**. Pictures of the drum-roll collector used to prepare the nanofibers are shown in **Figure S2**. **Figure 1b** and **Figure S3** show typical SEM images of the thus produced ternary blend-based fibers. As indicated by the orange and green arrows in **Figure 1b**, different thicknesses of the fibers can be observed. Two classes of thinner and thicker fibers are visible. From this image, 50 different diameters at the thicker fibers and 50 different diameters at thinner fibers were averaged by using the ImageJ software, to obtain individually the average fiber thickness of both classes. The average thickness of the thinner fibers (orange arrow) was calculated to be 159 nm, while the thicker ones have an average calculated diameter of 845 nm. These two trends in the distribution indicate that in some fibers the pure PEO component is prevailing, while in some of the others the presence of the three types of fillers is more concentrated and contributes to an expansion of the diameter. From the images, no preferential direction or, in other words, no directional order of the fibers created by the rotating motion of the drum-roll collector is visible. Therefore, we assume that the velocity of the accelerated fibers is larger than the rotating motion of the collector.

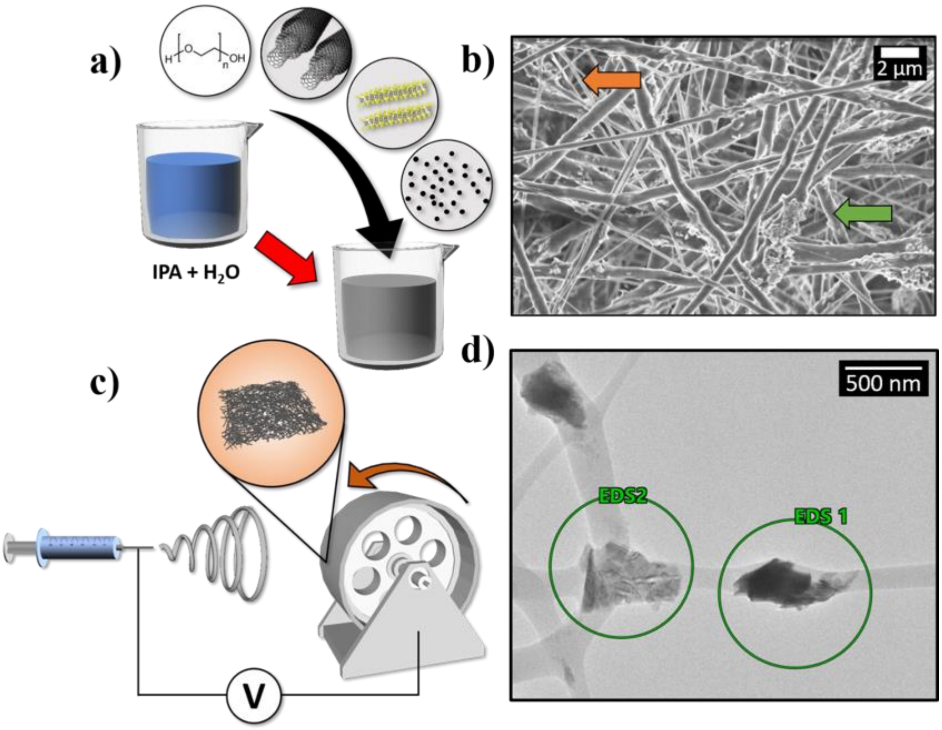

Figure 1. a) Schematics of blend composition, based on PEO (M_w = 1.000.000), functionalized MWCNTs, 2D-WS_2, and CB particles dissolved in an IPA/water mixture. b) Typical SEM image of the produced ternary blend-based fibers, with thicker fibers indicated by the green arrow and thinner fibers by the orange arrow. c) Schematics of the electrospinning process using a standard syringe and gathering the produced fibers on a drum roll current collector, by applying a potential between the syringe and the collector. d) STEM image of a single fiber deposited on a TEM grid, where EDS1 can be correlated to a carbon-based particle, while EDS2 is ascribed to an agglomerate of 2D-WS_2 sheets (see **Figure S4** for EDS spectra).

The produced fibers show a homogeneous distribution in the micro-meter scale of the layered WS_2 particles in the fibers, as proven by EDS analysis. In **Figure S3**, sulfur (light blue) and tungsten (pink) EDS signals are present throughout the entire image. TEM micrograph of the fibers (**Figure 1d**) shows two different spots where two different particle agglomerates are clearly visible in the fibrous material (the spectra for EDS1 and EDS2 are shown in **Figure S4**). The first spot (EDS1) can be ascribed to a carbon-based material, which can be either MWCNTs or CB added into the blends, since the carbon contribution is larger compared to the tungsten and sulfur contribution. The EDS2 measurement shows an agglomerate of several mono- or few-layer WS_2 sheets within the PEO matrix with an increased contribution attributed to tungsten and sulfur. From the insights of SEM and STEM images and their elemental analysis, it can be proved that layered WS_2 is present in the composite fibers.

Raman analysis was used to further characterize the presence of layered WS_2 in the produced fibers. Coleman et al. described the method for the LPE of 2D materials like TMDs.[24] The changes in band structure from indirect-to-direct bandgap were calculated and proven when going from the bulk to the mono- and few-layered WS_2 and MoS_2.[41,42] Raman spectroscopy can be used to differentiate between bulk and low-dimensional form, as it was described by Berkdemir et al.[43] Raman spectra of various WS_2 samples are shown in **Figure S5**. For the bulk material, the $(2LA + E_{2g})/A_{1g}$ ratio was observed to be 0.55 and 0.47 at an excitation wavelength of 514 nm and 514.5 nm, respectively.[43,44] Since the measurements were carried out at 532 nm excitation wavelength, and the sensitivity for the number of layers and the effect on the spectra depend on the excitation wavelength, bulk WS_2 was used as a reference to compare the degree of exfoliation to the literature.[43,45] **Figure S5** confirms that the literature-reported values are in agreement with the experimentally obtained ratio of $(2LA + E_{2g})/A_{1g} = 0.499$ from the reference bulk WS_2 powder. Therefore, the $(2LA + E_{2g})/A_{1g}$ ratio at 532 nm remains a suitable proof of the exfoliation degree. The single sheets always possess $(2LA + E_{2g})/A_{1g}$ ratios above 2, while double layers achieve ratios around 1.[43,46] As **Figure S6** shows, all measured spectra that contain WS_2 feature ratios far above 1, with 1.34 for the binary fibers containing functionalized MWCNTs and WS_2, 1.74 for the fibers containing only WS_2, which means that in these fibers mainly double- and monolayers of the TMD are present. For the ternary fibers, a ratio of 2.08 results from Raman peaks analysis, indicating that the WS_2 particles predominantly exist as monolayers in this sample[18] In the range between 1250 cm^{-1} and 1700 cm^{-1}, the detection of MWCNTs was also possible. As also indicated in **Figure S6**, D- and E_{2g}-bands of carbon are found at Raman shifts of 1352 cm^{-1} and 1585 cm^{-1}, respectively. The D-band position (1352 cm^{-1}) strongly depends on the utilized excitation wavelength and shifts towards larger wavenumbers with increasing excitation energy: this can be attributed to electronic states emerging in disordered graphitic materials that couple resonantly with the excitation laser, causing the observed wavelength-depending shifts.[47,48] However, it is clear that MWCNTs are present in all samples by looking at E_{2g}- and D-bands, except for the PEO-2D-WS_2 sample, which does not contain them. The low intensity, large defect concentration, and the poor ratio between the two bands I_{E2g}/I_D results from different causes. The first effect is caused by the overall concentration of the MWCNTs in the prepared suspension, being low compared to the other components (around 1.28 wt%), which is why WS_2 signals simply dominate the spectra. The comparably large defect band is caused by the utilized MWCNTs. For a better dissolution in the water/IPA mixture, functionalized MWCNTs with carboxylic acid were used. As a consequence, more defects are present on the nanotube surface disturbing the graphitic order, which is the main reason for the low-intensity E_{2g}-band contribution resulting in the poor, above described, ratio.[47,49]

Figure S7 displays the XRD patterns of all different PEO-based nanofibers that were produced from the prepared blends. PEO fibers naturally show a certain crystallinity after the electrospinning process, which is seen throughout all different samples. [50,51] In 2001, Deitzel et al. ascribed the reflexes (indicated as the red dots) directly to the crystalline phase of PEO.[27] Besides the comparably small reflexes of PEO, larger relative intensities can be ascribed to WS_2 reflexes, and there is no doubt that crystalline WS_2 is present in the fibers originated from the 2D-WS_2-containing blends (indicated by the blue rectangles in **Figure S7**). The (002) reflex at 14.3° (d_{002} = 1.01053 Å) from the reference is the most prominent reflex for the 2H-phase of the TMD. No side phases, such as WO_3 or 1T-WS_2, were produced during exfoliation and fiber-spinning. In the case of WS_2, the exfoliation might affect the reflex position and, further, the d-spacing of layers. The deviation of the reflex positions for all samples corresponds, compared to the reference, to d-spacing differences from 0.0051% to 0.8447%. The exfoliation of bulk WS_2, dissolved in suspensions and finally electrospun, therefore, did not affect the distance of the d_{002} plane of the 2H-WS_2 phase and no phase transitions were observed.

The electrochemical characterization of the composite fibers, aimed at determining the most performing composition in terms of fillers type and quantity, was carried out through CV in a Swagelok cell-type device (see **Figure S8**) by using a non-aqueous electrolyte. Due to the polar nature of PEO, which is soluble in most typical solvents used for electrolytes, PC, a high boiling, non-polar solvent was used for dissolving $TEABF_4$, which acts as the charge transferring species (electrolyte) within the electrochemical cell. Different blends with increasing concentrations of MWCNTs and 2D-WS_2 as shown in **Figures 2a** and **b** were produced and analysed. From the CV traces (**Figure S9**) the specific capacitance was calculated by using the following equation[52,53]:

$$C_s = \frac{A}{\Delta V \cdot \nu \cdot m}$$

where C_s is the specific capacitance, m is the sample mass in grams, ΔV is the potential window, v is the scan rate in mV s^{-1}, and A is the area of the voltammograms in **Figure S9**. The potential window was chosen between -0.25 V to 0.6 V, which was found to be the non-Faradic region for the composite fibers. Since referring this material system to a reference electrode is difficult due to the high solubility of PEO in aqueous solvents, a pseudo reference (ferrocene) was used to be able to contextualise the applied potential window. **Figure S10** shows the anodic and cathodic peaks of the ferrocene couple (Fc/Fc^+) in the used electrolyte system of $TEABF_4$ and PC at 0.5 M concentration. The offset potential can be derived from the middle of the two peak potentials. The offset of 0.74 V, which is obtained from these curves, is then subtracted from the applied potential and corresponds to the potential range -0.99 V to -0.14 V *vs* Fc/Fc^+ shown in **Figure S9**. Inside this region, no redox reactions are occurring, measured currents are a consequence of surface charging instead of electrochemical reactions, which enables the determination of C_s. By adding more charge-conductive species, namely MWCNTs and 2D-WS_2, intuitively the capacitance of the fabricated fibers should increase. A larger concentration should enable a larger C_s, since more active material is present for charge storage. However, there is no such trend visible in the obtained data summarized in **Table S1**. With increasing scan rates, the size of the diffusion layer decreases, due to the electrolyte diffusion towards the electrode, which explains the overall larger currents shown in **Figure S9**.[54] For all samples, but especially for the PEO-WS_2 and PEO-WS_2-MWCNTs-CB composites, a rectangular shape is measured, proving the capacitive behaviour. The overall shrinking of C_s, with raising the scan rate, has its origin in the diffusion limitation of charges into the material and is commonly seen for CV-type measurements.[38] Therefore, the obtained values discussed from now on are the ones measured at a scan rate of 10 mV s^{-1} (**Figure S9**). Again, for optimization of concentrations of 2D-WS_2 and MWCNTs in the fibers, the 2D-WS_2-PEO and MWCNTs-PEO were measured in the Swagelok cells in **Figures 2a** and **2b**. It was obtained that, by doubling the concentrations to 25 mg mL^{-1} for WS_2 and 1 mg mL^{-1} for MWCNTs, a rapid drop of the specific capacitance from 20.06 mF g^{-1} to 8.69 mF g^{-1} in the case of 2D-WS_2 and from 27.47 mF g^{-1} to 8.03 mF g^{-1} for the MWCNTs containing fibers was obtained, as visualized in **Figures 2c** and **d**. Afterwards, at a concentration of 37.5 mg mL^{-1} for 2D-WS_2 and at 1.5 mg mL^{-1} for MWCNTs, the specific capacitance increases again to 12.24 mF g^{-1} for 2D-WS_2 and up to 22.22 mF g^{-1} in the case of MWCNTs fibers. Due to the insolubility issues, there is a limit to the amount of material that can be added to the suspensions for each species, which was reached or exceeded at these concentrations of 1.5 mg mL^{-1} for MWCNTs and 37.5 mg mL^{-1} for WS_2. The particles of 2D-WS_2 and carbon species, which are present in the blends shown in **Figure 1b** and **Figure 1d**, have lateral sizes around 500 nm up to a few μm. By adding more of these large particles into the blends, homogeneity cannot be longer ensured. We observed that high concentrations lead to poor dispersion and agglomeration and that the overall distribution of 2D-WS_2 and MWCNTs in the fibers becomes worse compared to blends with lower concentrations.

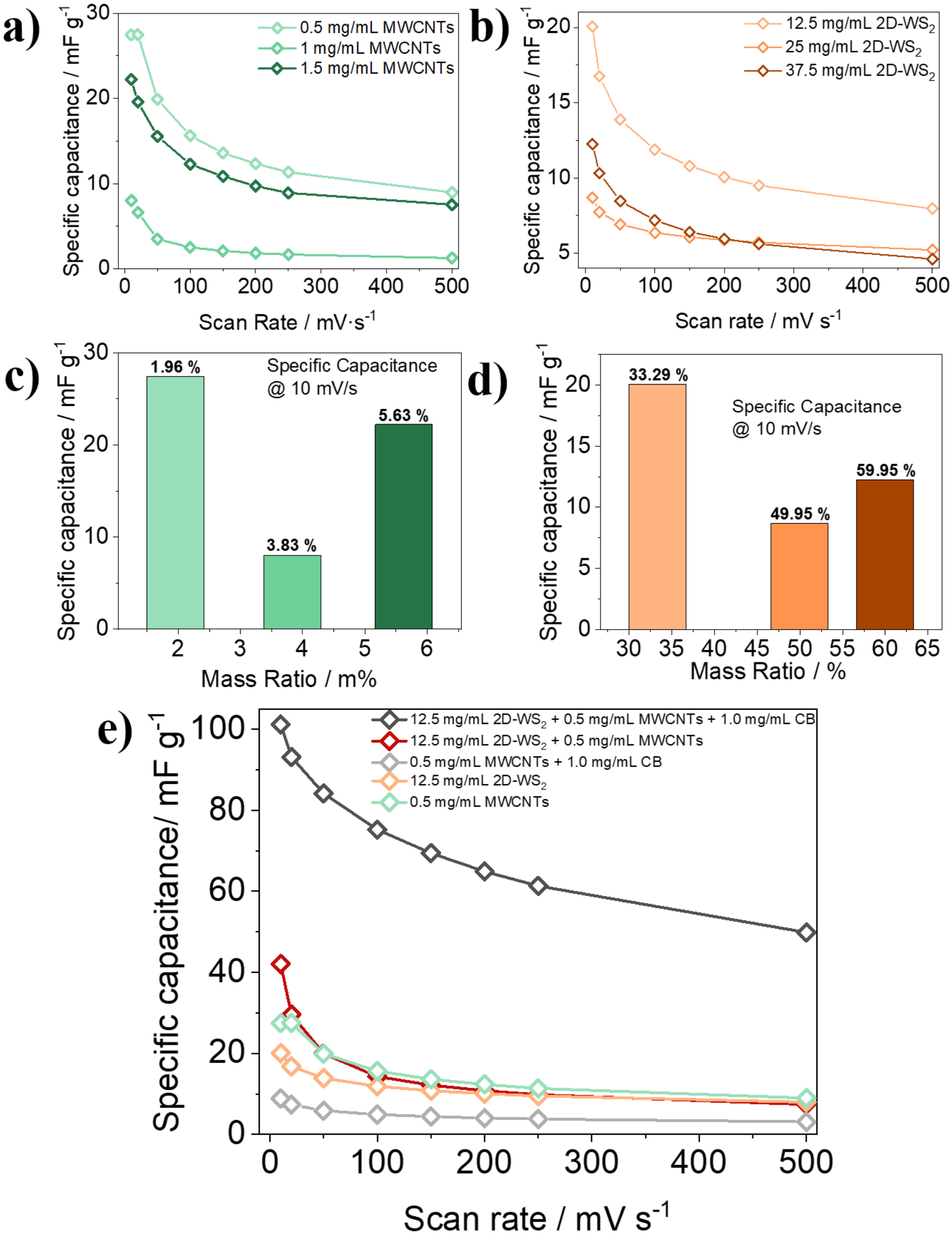

Figure 2. C_s for differing concentrations of **a)** PEO-MWCNTs fibers from 0.5 to 1.5 mg mL^{-1} and **b)** 2D-WS$_2$ from 12.5 to 37.5 mg mL^{-1}. **c)** and **d)** show the C_s vs. mass ratio in % at a scan rate of 10 mV s^{-1} for 2D-WS$_2$-PEO fibers and MWCNTs-fibers. **e)** Data for the best performing samples from **a)** and **b)**, i.e. for, fibers containing MWCNTs-CB at a concentration of 0.5 mg mL^{-1} for MWCNTs and 1 mg mL^{-1} for CB, the mixture of 2D-WS$_2$ and MWCNTs with

optimized concentrations (dark red), and the mixture of both additives at optimized concentrations, including the addition of CB at a concentration of 1 mg mL^{-1}. The measurements were done in a Swagelok electrochemical cell using $TEABF_4$ at a concentration of 0.5 M dissolved in PC as electrolyte. The measurements were done at 10 mV s^{-1}, 20 mV s^{-1}, 50 mV s^{-1}, 100 mV s^{-1}, 150 mV s^{-1}, 200 mV s^{-1}, 250 mV s^{-1}, and 500 mV s^{-1} in a range between -0.25 and 0.6 V (non-Faradic region).

In **Figure 2e**, the mixture of the best-performing concentrations from **Figure 2a** and **b** are reported, together with the binary composites of 2D-WS_2-MWCNTs, as well as the composite of MWCNTs-CB. It is important to underline that fibrous samples with binary composition 2D-WS_2 + CB do not appear among the ones tested in **Figure 2e**. The CB-based fibers not containing all the three additives together provided too inhomogeneous mats, which were not possible to remove from the aluminium foil after the electrospinning deposition process, making their electrochemical characterization not feasible. In contrast, the ternary mixture is clearly outpacing all the investigated binary and mono-filler compositions, with a remarkable value of C_s reaching almost 100 mF g^{-1} at the slowest utilized scan rate and decreasing to 50% of this value at the fastest one. Electrical conductivity measurements prove that the addition of CB contributes mainly to a decrease in resistance, as it can be seen in **Figure S11**. Due to a lack of mechanical stability, also fibers produced from a simple PEO-CB blend were not studied electrochemically, due to inability of detaching them from the collector foil in the electrospinning set-up. The composite fibers based on binary 2D-WS_2-MWCNTs mixture in PEO show an increase of the electrochemical performance up to 42.05 mF g^{-1} compared to the reference fibers with only one of the two fillers, demonstrating a beneficial cooperative effect between the two nanomaterials. Notably, a binary blend of MWCNTs and CB in PEO, at the same concentration kept in the ternary one, shows poor electrochemical performance, other that being a very brittle and electrostatic sample, with incompatible mechanical properties for use in flexible device architectures. These fibers appear inhomogeneous, which is most likely caused by agglomeration of the carbon fillers. Therefore, clogging of the syringe tip while electrospinning is expected, resulting in low fiber stability and inhomogeneous distribution of active species. Consequently, a reduced number of conductive paths through the fibrous matrix is formed, triggering low capacitive performance. In the ternary composite instead, where CB was added to improve electrical conductivity, the strong enhancement in C_s suggests a beneficial interaction between 2D-WS_2 and the carbon species, which are consequently better distributed in the fibrous polymer matrix, as long as 2D-WS_2 is present.

We investigated the mechanical properties of the prepared nanocomposite fibers, to prove their suitability for use in flexible devices. Mechanically, the fibrous mats show different properties, depending on the specific filler they contain. Therefore, their UTS, YM, and EB were measured to test their resilience against mechanical stress. Especially the values of YM and EB play a crucial role in their use in flexible electronics and supercapacitors: the active material should not break and remain in its former shape when slightly bent. Since the fibers are spun on a rotating drum roll collector, the influence of the spinning process itself was investigated by measuring at least 10 samples along the spinning direction (longitudinal) and perpendicular to the spinning direction (transversal). As shown in **Figure S12**, it was noticed how the position on the mats, where the samples were gathered, influenced their mechanical behaviour: the closer to the edges they were the lower their maximum tensile stress was. Indeed, while electrospinning, the needle tip is positioned in the centre of the drum collector and, therefore, fibers mats are centrally loaded and their thickness decrease as far away from the centre. For this reason, samples were cut from the middle of the fiber-mats to perform longitudinal measurements. Even if an orientation of fibers on the rotating collector was expected at first, the SEM images reported in **Figure 1b** and **Figure S3** did not show a preferential direction, which was explained by the low rotation speed. Since distances of 25 cm were used for producing the fibers and large acceleration voltages were present, the fibers reached the collector quickly. Within that time, the collector itself did not rotate a large distance since it was rotating at 60 rpm. This result is in agreement with a previous work by Kumar et al.[55], where, to obtain aligned fibrous material, up to 2500 rpm were needed, while 300 rpm resulted in non-aligned fibers. Representative stress-strain curves of longitudinal and transversal samples for each filler mixture are shown in **Figure 3a** and **Figure 3b**, respectively. One exception is the PEO-CB sample. As mentioned before, the CB-based fibers without all three fillers featured poor homogeneity and, thus, no delamination from the aluminium foil was possible without damaging the mats. As a consequence, their characterization could not be conducted. As it can be noticed, from the comparison of the longitudinal samples (**Figure 3a**), an effective increase of the maximum tensile stress was observed in presence of carbon-based fillers, whereas all the other fillers did not bring any improvement.

On the other hand, transversal samples (**Figure 3b**) did not show any difference in maximum tensile stress depending on the filler involved in the formulation. Therefore, only PEO-WS_2-MWCNTs-CB composite showed a significant different in maximum tensile stress: a 40 % reduction was observed from longitudinal to transversal samples. Mechanical properties of the composites were investigated in terms of YM, EB and UTS and results are reported in **Table 1**.

Table 1. YM (MPa), EAB (%), and UTS (MPa) of PEO, PEO WS_2, PEO MWCNTs, and PEO-WS_2- MWCNTs-CB. All the data are reported as average ± standard deviation. ANOVA test ($p<0.05$).

	PEO	**PEO:2D-WS_2**	**PEO:MWCNTs**	**PEO:2D-WS_2:MWCNTs:CB**
YM – Long. (MPa)	61.00 ± 16.71	42.99±11.92	97.40±17.69	96.47±31.90
YM – Trans. (MPa)	60.33 ± 16.50	40.87±9.40	81.63±21.13	77.87±12.17
EB – Long. (%)	195.07 ± 74.64	208.69 ± 34.95	95.57 ± 13.21	139.04 ± 31.68
EB – Trans. (%)	136.60 ± 25.56	96.00 ± 40.43	78.18 ± 17.63	56.03 ± 15.79
UTS – Long. (MPa)	4.78 ± 0.81	5.33 ± 0.97	4.90 ± 0.31	7.11 ± 1.17
UTS – Trans. (MPa)	4.54 ± 0.39	3.68 ± 0.95	5.12 ± 0.26	2.75 ± 0.22

As it can be noticed, both the YM (**Figure 3d**) and the EB (**Figure 3c**) of samples containing MWCNTs significantly differed from samples without MWCNTs, regardless of the longitudinal or transversal direction. Indeed, the YM of pure PEO increased from (61.00 ± 16.71) MPa up to (97.40 ± 17.69) MPa for PEO-MWCNTs. The addition of WS_2 and CB to PEO-MWCNTs did not show a change in the YM (96.47 ± 31.90) MPa. Therefore, it could be stated that the improvement of the YM of the pure PEO was only due to the MWCNTs. Indeed, MWCNTs are significantly more rigid than PEO, with a YM in the range of 270–950 GPa, as measured by Yu et al.[12] Furthermore, the UTS data (**Table 1**) did not show significant changes in pure PEO after the addition of all the fillers. The maximum value in the longitudinal direction was obtained by the ternary blend-based fibers with (7.11 ± 1.17) MPa, while the transversal direction was lacking in strength with just (2.75 ± 0.22) MPa performing worse compared to all other samples. The values for MWCNTs-filled fibers differ from samples without MWCNTs. On the other hand, as expected, since the fibers are mechanically strengthened due to the nanotube addition, a decrease in the EB was observed;[31] conversely, pure PEO and PEO-WS_2

fibers, showed EB 195 and 209% in the longitudinal direction and ~96-137% in the transversal direction. The EB of PEO-MWCNT and PEO-WS_2-MWCNTs-CB composites showed a significant decrease with 96% and 139%, respectively, in the longitudinal direction, and 78% and 56% in the transversal direction (**Figure 3c**).

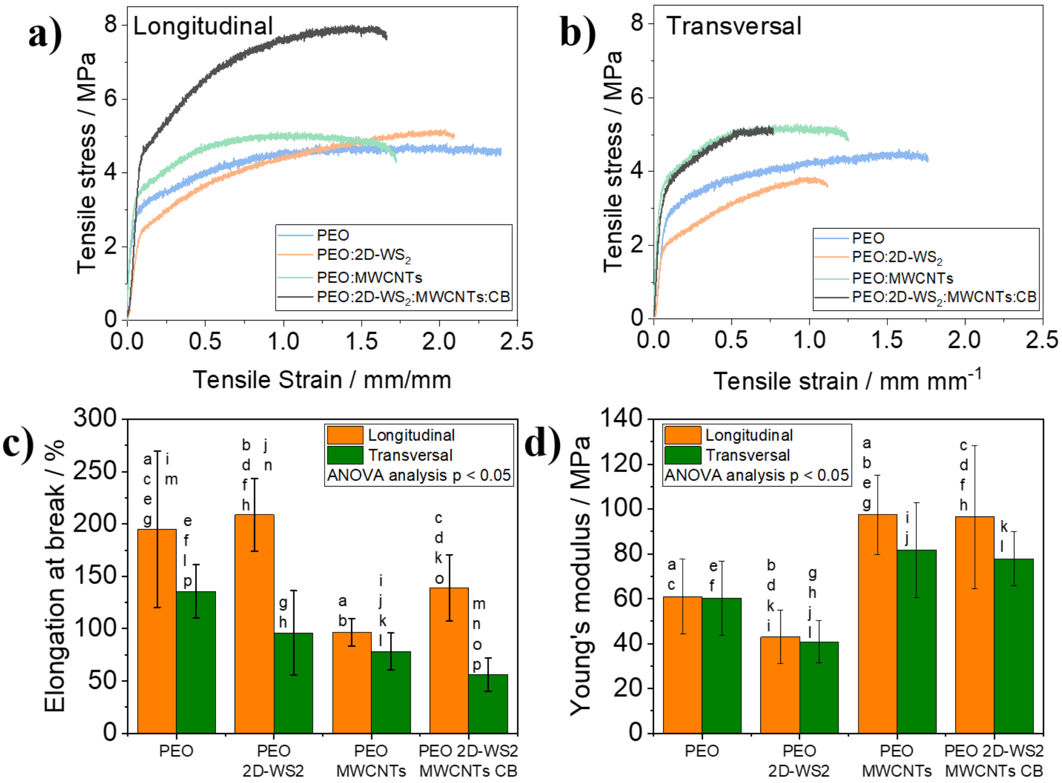

Figure 3: Representative stress-strain curves of pure PEO (light blue), PEO-WS_2 (light orange), PEO-MWCNTs (dark red), PEO-WS_2-MWCNTs-CB (black) in (**a**) longitudinal direction and (**b**) transversal direction. The average values of the EB and the error bars for all samples are shown in (**c**) with the added letters for the statistical analysis from ANOVA with a p-value of 0.05. If the p-value is above 0.05, there is a significant difference in the two compared data sets. This difference is indicated with a letter in the diagrams showing that the two data sets are significantly different. The average values of the YM and the error bars for all samples are shown in (**d**) with the added letters for the statistical analysis from ANOVA with a p-value of 0.05. The explicit values for (**c**) and (**d**) can be found in **Table 1**.

Theoretically, MWCNTs length of 1.5 µm is in a range where the tubes align along the produced PEO fibers (100–900 nm) and effectively contribute to the strength of the fibers.[31] Adding fillers, except for the MWCNTs with a comparably high tensile strength, the fibrous materials are weakened, most likely due to a limited dispersity of CB and 2D-WS_2. The EB suffered less because of CB and 2D-WS_2 fillers. In contradiction to what was initially expected, throughout the whole set of samples an anisotropic behaviour was observed because the transversal direction significantly differs from the longitudinal direction with a lower elongation and with withstanding higher loads before breaking. Most likely this can be ascribed to the deposition along the rotation axis of the current collector used in the electrospinning process: even if initially thought the low rotation speed of the drum roll collector has no influence, it can be assumed that fibers are slightly aligned, unnoticeably by only watching at SEM images. The weakness of the transversal direction cannot be explained by the observed gradient of thickness, even if the sample position could not be adjusted like in the case of the longitudinal direction (see **Figure S12**) the total width of the drum roll was 10 cm, while the length of the cut samples was 2.5 cm and taken from the middle of the mats.

To characterize thermal stability, TGA was carried out on the composite fibrous materials and the thermograms are shown in **Figure S13**. For any filler added, an increase in the degradation temperature of PEO was observed. Bare PEO-fibers started rapidly decomposing at a temperature of 141 °C. By adding 0.5 wt% of MWCNTs, the decomposition temperature was raised up to 171 °C. Surprisingly, the PEO-WS_2 composite fibers obtained the overall largest burning temperature with 264 °C. The mixture of PEO-WS_2-MWCNTs was decomposed at 185 °C, while the ternary blend-based fibers at 256 °C. At first it is important to mention that the influence of WS_2 is the largest for all samples. This is simply because of the chosen mass ratios of the mixtures (PEO:WS_2:MWCNTs:CB = 50:25:1:2), therefore WS_2 should naturally show a stronger effect. This can be seen at the remaining mass at 700 °C, which is mainly ascribed to the WO_3 mass, since all samples that do not contain WS_2 have significantly lower masses. This means that the lower the relative ratio of PEO, the higher the burning temperature. The only exception is the PEO-WS_2 sample. One possible explanation could be the agglomeration of the filler species inside the fibers. As shown in **Figure 1d**, most likely agglomerates of WS_2 and CB or MWCNTs appear in the produced blends and prevent more homogeneous mixing. Then, a lower amount of PEO is interacting with the WS_2 surface because the carbon species block access to the latter. Since WS_2 can trap positive charges, numerous partial negative charges along the PEO chain interact with the WS_2 surface.[37] This weak interaction of PEO chains might cause larger temperatures for decomposing PEO close to WS_2 particles. This could be highlighted by looking at the position of the ending of the mass drop in TGA data. The ternary blend-based mixture and the binary PEO-WS_2-MWCNTs composite show a rapid drop until 305–315 °C, while this state is reached around 360 °C for the PEO-WS_2 fibers. For decomposing residual PEO, close to the WS_2 particles, larger temperatures are necessary due to the PEO-WS_2 interactions. However, previously it was found that metal oxide-

WS_2 composites were able to effectively act as flame retardant for polyethylene implemented in a PE matrix: we also observed a comparable trend the produced WS_2-based composite fibers from PEO.[56]

After optimizing the concentration for each additive in the composite fibers, a flexible current collector was used as a substrate for direct fibers spinning, in order to prepare the two main parts of a flexible symmetric supercapacitor. CB and PTFE were used to produce the current collector (CB-PTFE CC) used as a substrate (**Figure S2**), as described in the Experimental Section. PEIS was employed to characterize the electrical performance of the CB-PTFE CC. From these flexible substrates and the on-top deposited fibrous mats, pouch cell devices were fabricated as explained in the Experimental Section and shown in **Figure 4a**. As it can be deduced from **Figure S14** and **Table S2**, PEIS measurements on CB-PTFE CC provide a resistance of 172 Ω with a double-layer capacitance of 2.6 nF, using a fitting model based on a Randles' circuit, which is an acceptable value for a flexible CC featuring electrical conductivity and some capacitive behaviour as well.[57] **Table S1** summarizes the values obtained from the experiments in **Figure S15** of the assembled pouch cells, as well as from the data shown in **Figure 4b**. From **Figure S15**, it can be seen that the pure CB-PTFE CC shows a specific capacitance of 0.49 F g^{-1}, which is a factor 4.65 larger than the ternary fibers measured in the Swagelok cell. The composite being produced from the CB-PTFE CC and the ternary fibers in **Figure 4b** (yellow graph) already shows a large increase of the specific capacitance up to 3.54 F g^{-1}. This drastic enlargement can be explained by several reasons. At first, as the reference in **Figure S15** shows, there is a contribution of the CB-based current collector. It is well known in the literature, especially for Li-ion and Na-ion batteries, that CB acts as a capacitive species.[58,59] Additionally, CB affects the conductivity of the composite material. CB as a conductive material enables charge transport to the electrodes, as the diagram in **Figure S11** indicates, while **Figure S2** shows the ability of the substrate to conduct current and sustain a commercial LED. The aforementioned direct-spinning process onto the CB-PTFE CC likely leads to good contact between the fibers and the conductive current collector. The decreased distance that charges have to overcome during the charge-discharge process in the PEO-based matrix is way more probable when more contact points to the electrode material are present. Furthermore, the vacuum treatment used to produce pouch cells compresses the fibers as well as the separator with overall densification of the cell structure. Being the distance between two electrodes in the capacitor reduced, C_s becomes logically higher, given the inverse proportionality.

The device with the best performance was used to conduct cyclability tests using capacitance retention measurements. Galvanostatic charge-discharge measurements were performed for

3000 cycles at a current density of 50 mA g^{-1} (**Figure S16**). C_s retention was found to be very effective and the C_s was maintained constant over 3000 cycles, reaching up to 102.3% of the initial value. Coulombic efficiency also remained constant for 2000 cycles and then slightly shifted upwards to a maximum value of 107.1%. This upward trend is known especially for carbon-based materials, where self-activation takes place by changes in the surface morphology concomitant with an increase in the specific surface area during successive electrolyte permeation cycles. Additionally, during cycling, some electrochemically active sites become better exposed to the electrolyte.[60,61] Overall, the constant performance for 3000 cycles shows that under cycling conditions no degradation or parasitic chemical reactions in the system occur and that excellent stability of the composite-electrolyte system in the device is ensured.

Figure 4b discloses another beneficial effect to the specific capacitance: for flexible materials, the bending tests are highly relevant. To test the stability of a flexible supercapacitor, the active species within it must withstand several cycles of bending (at least 10). After the first bending cycle, C_s of the cell is even raised up to 12.019 F g^{-1}. While bending pressure is applied to the cell, the internal components are compressed, which is beneficial for improving the contact among the different species. This effect also explains the differences observed when employing the same active materials (the fibrous mats) in different cell geometries, namely Swagelok and pouch cells. By vacuum sealing, a pouch cell is most likely more compressed compared to a Swagelok cell.

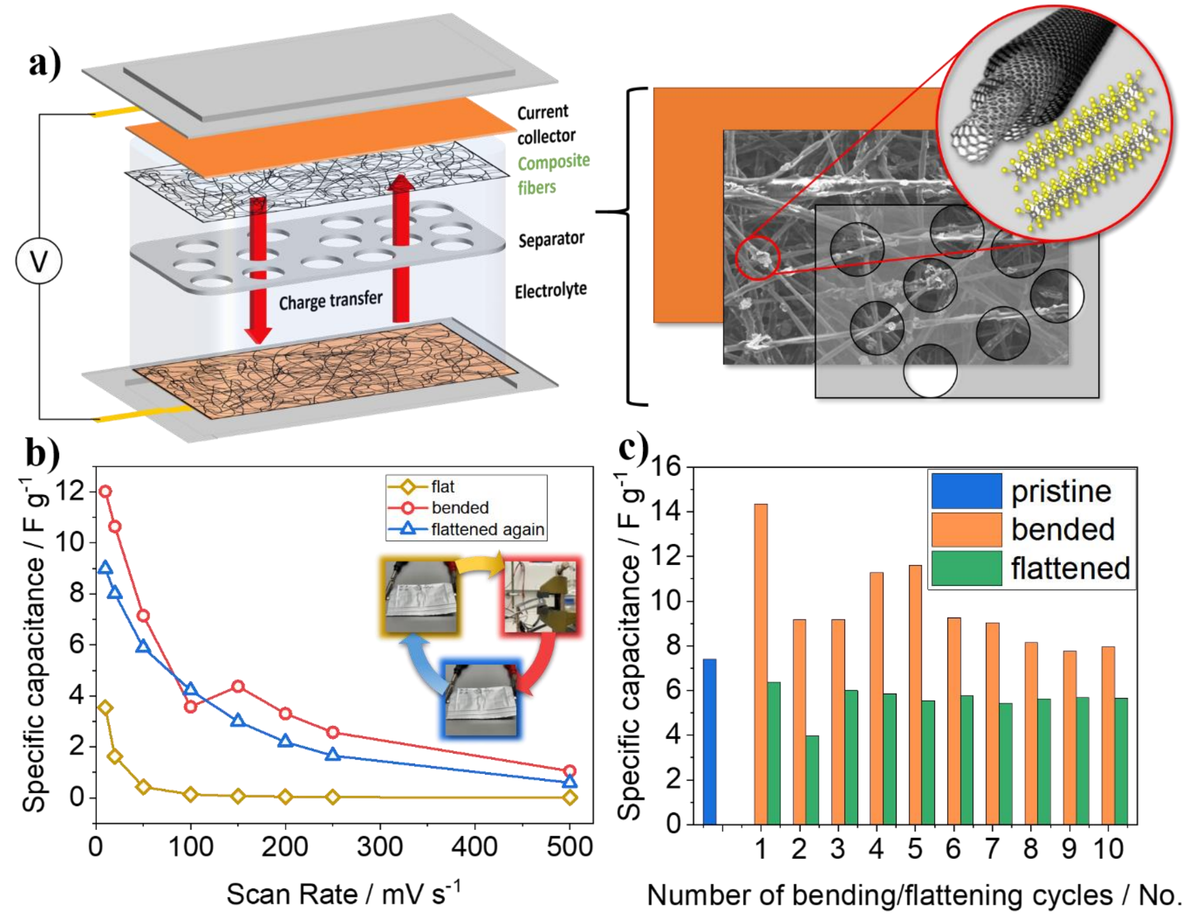

Figure 4. a) Schematic of pouch cell architecture for the symmetric supercapacitor devices used for electrochemical analysis. The pouch cells are built using nickel tabs as current conductors, CB-PTFE coated with the ternary blend-based fibers and a SiO_2 fibrous membrane (Whatman) as a separator. 120 µL of 1 M $TEABF_4$ dissolved in PC was used as electrolyte. The measurements were done at 10 mV s^{-1}, 20 mV s^{-1}, 50 mV s^{-1}, 100 mV s^{-1}, 150 mV s^{-1}, 200 mV s^{-1}, 250 mV s^{-1}, and 500 mV s^{-1} in a range from -0.25 to 0.6 V. Panel **b)** shows the specific capacitance depending on the scan rate before bending (yellow), during the first bending (red), and after the first bending (blue). The inlet visualizes the bending process. In **c)** Another symmetric cell (different sample from the one used in b) was bent 10 times and the specific capacitance was measured in the bent as well as in the flat state at a scan rate of 10 mV s^{-1}.

Consequently, in the latter, stored charges are hindered to flow from the PEO fibers-based matrix into the current collector since less contact with the current collector exists in this architecture. This effect was also observed for lithium-ion pouch cells by Zhou et al., where - with increasing pressure - a decreasing internal resistance was observed, while the capacity was increasing.[62] Additionally, they also observed an irreversible increase of the capacitance even after removing pressurization, which is also seen in our samples after flattening in **Figure 4b** (blue curve). A decrease compared to the bent (pressurized) state of the C_s is observed (8.992 F g^{-1}), but nonetheless it still remains larger compared to the initially prepared cell. The downward trend in C_s at 100 mV s^{-1} seen after the first bending cycle (red curve), followed by an increase at 150 mV s^{-1}, becomes understandable by looking at **Figure 4c**. In the bent configuration, fluctuations of C_s are always present, mainly caused by the change in pressure in the cell (not controlled here, but done manually), which affects the distance of the two electrodes from each other and the electrolyte penetration. In the flat state, almost no fluctuations of C_s can be noticed. The stability tests in **Figure 4c** conducted on another device show the same upward trend on the first bending cycles. Depending on the cycle, C_s varies from a maximum of 14.35 F g^{-1} to a minimum of 7.77 F g^{-1} in the bent configuration. This is explained by the bending process itself. By hand, the pressure applied to the cell will always differ from one bending cycle to another. However, after three cycles of bending, a plateau of around 5.70 F g^{-1} can be observed. This means that pressurization reaches an equilibrium state where the capacitance remains more or less constant independent from the previous bent state.

We have compared our results with those of similar devices reported in the literature, mostly flexible supercapacitors based on carbon materials, polymers and TMD-based composites. Lamberti et al. produced laser-induced, flexible graphene sheets, which in device provided 0.2 mF cm^{-2} at a scan rate of 10 mV s^{-1}.[63] Also Peng et al. obtained 9.11 mF cm^{-2} at a current density of 0.5 mA cm^{-2} with a similar laser-induced flexible graphene material. In comparison, the areal capacitance of the composite fibers reported in this work achieves values of 107.7 mF cm^{-2} at a scan rate of 10 mV s^{-1}, which is comparable or even better than the two cited cases. Zhou et al. prepared graphite papers using the exfoliation technique and obtain 101.5 mF cm^{-2} at a current density of 0.5 mA cm^{-2}, a value close to the one here presented.[8] More comparable with our architecture, a polymeric flexible system made of polypyrrole-stabilized polypeptides achieved 42 mF cm^{-2} (4 F g^{-1}) at a current density of 0.2 mA cm^{-2}, with our material featuring 5.70 F g^{-1} after 10 bending cycles at 10 mV s^{-1}.[7] Sun et al. presented a hybrid TMDC-carbon-based fiber material from MoS_2, reduced graphene oxide and MWCNTs and obtained 4.8 F cm^{-3} at a current density of 0.5 A cm^{-3}. Roughly assuming a thickness of 0.02 cm for our composite electrode, we obtain a volumetric capacitance of 5.39 F cm^{-3} at the scan rate of 10 mV s^{-1}.[64] Here, our material performs better or comparably to several published examples. From carbon-based materials there are also works, especially in the field of CNFs, reporting larger C_s: in our previous work on CNFs, we reached 49 F g^{-1} at 0.5 A g^{-1}, while in other examples activated CNFs provided 83.3 F g^{-1} at a current density of 100 mA g^{-1} or 95 F g^{-1} at a scan rate of 10 mV

s^{-1}.[10,21,36] However, it is worthy to remind that most CNF-based electrodes have limited flexibility, which makes them unsuitable for application in flexible energy storage devices.

4. Conclusion

In this work, we studied the effect on the electrochemical and mechanical performances of nano-engineering electrospun PEO nanofibers with layered WS_2, MWCNTs and CB. The described achievements suggest that a capacitive behaviour is clearly present in the composite material, with C_s values up to 0.1 F g^{-1} at 10 mV s^{-1} scan rate. It is important to note that this quantity does not derive from the simple sum of each individual component contribution, but comes from a synergistic effect of the three different nanostructures, assembled in an optimized way within the fibrous scaffold. In fact, the structural characterizations performed (XRD, SEM and TEM), coupled to thermogravimetric analysis, show an intimate contact between the nanomaterials, which justifies the establishment of cooperative effects in the transport and storage of electrical charges. The mechanical properties are also influenced by the presence of the nanofillers, with improved figures of merit and, notably, an increased UTS when CB is present and a 60% boosted YM boosted when MWCNTs are used, whereas EB is substantially reduced.

As proof of concept to demonstrate the potential for integration into flexible energy storage devices, we show the fabrication of a flexible symmetric capacitor and test it ability to maintain a good capacitance after multiple cycles of bending and re-flattening, with only about 25% loss of the initial C_s after 10 cycles, that suggest how the plastic behaviour of the device is supported by the effective mutual cooperation of its nano-components.

These findings reveal the impact of nano-engineering polymeric matrices with electrically active fillers to pave the way to new functional materials, which will promote a step-forward in the ideation of versatile energy storage units for low-power electronics embedded within portable and light-weight technologies.

Supporting Information

- Schematic description of the production of 2D WS_2 powder, MWCNTs suspension, and steps for the preparation of the ternary blend (**Figure S1**)
- Conductivity and flexibility tests on CB-PTFE mats and electrospinning process of polymer fibers onto the CB-PTFE mats (**Figure S2**)
- SEM and EDS images of fibers produced from the ternary blends (**Figure S3**)
- EDS spectra of two particles found in the ternary fibers (**Figure S4**)

- Raman spectra of the WS_2 bulk reference, produced 2D WS_2 powder and re-dispersed 2D WS_2 (**Figure S5**)
- Raman analysis and spectra of various fibrous materials containing different mixtures of additives, including an inset magnifying the region of Raman shifts in the region of MWCNTs (**Figure S6**)
- Diffractograms of various fibrous materials containing different mixtures of additives with the given reflexes for WS_2 and PEO (**Figure S7**)
- Schematic of the Swagelok-cell used for electrochemical characterization in a symmetrical supercapacitor configuration (**Figure S8**)
- CV scans on fibrous materials at the optimized additive concentrations at different scan rates (**Figure S9**)
- Ferrocene redox reaction in 0.5 M $TEABF_4$/PC electrolyte (**Figure S10**)
- Values of all calculated C_s from the CV curves at different scan rates shown in **Figures 2**, **4b** and **S15** (**Table S1**)
- Conductivity measurements done on pellets of fibrous mats (**Figure S11**)
- Dependency of stress-strain curves from the position on the fiber mat shown for fibrous mats of the PEO-WS_2 composite material (**Figure S12**)
- Thermogravimetric analysis of all produced fiber samples (**Figure S13**)
- Schematic of the Swagelok-cell PEIS measurements on CB-PTFE mats with the corresponding Randles' circuit. (**Figure S14**)
- Values, error-values, and error in percentage for the serial resistance, charge transfer resistance, and double layer capacitance calculated from the PEIS measurements of the DB-PTFE mats (**Table S2**)
- C_s from CV curves using pouch cells of CB-PTFE current collector and the composite with ternary fibers in a symmetrical supercapacitor configuration (**Figure S15**)
- C_s retention tests carried out using galvanostatic charge-discharge cycles on a pouch cell at 50 mA g^{-1} for 3000 cycles. (**Figure S16**)

Acknowledgment

F.B., M.C., B.S., and T.G. wish to thank the financial support of the European Commission through the H2020 FET-PROACTIVE-EIC-07-2020 project LIGHT-CAP (project number 101017821).

References

(1) Ding, Y.; Xu, W.; Wang, W.; Fong, H.; Zhu, Z. Scalable and Facile Preparation of Highly

Stretchable Electrospun PEDOT:PSS@PU Fibrous Nonwovens toward Wearable Conductive Textile Applications. *ACS Appl. Mater. Interfaces* **2017**, *9* (35), 30014–30023. https://doi.org/10.1021/acsami.7b06726.

(2) Jin, L.; Wang, T.; Feng, Z. Q.; Leach, M. K.; Wu, J.; Mo, S.; Jiang, Q. A Facile Approach for the Fabrication of Core-Shell PEDOT Nanofiber Mats with Superior Mechanical Properties and Biocompatibility. *J. Mater. Chem. B* **2013**, *1* (13), 1818–1825. https://doi.org/10.1039/c3tb00448a.

(3) Choi, J.; Lee, J.; Choi, J.; Jung, D.; Shim, S. E. Electrospun PEDOT:PSS/PVP Nanofibers as the Chemiresistor in Chemical Vapour Sensing. *Synth. Met.* **2010**, *160* (13–14), 1415–1421. https://doi.org/10.1016/j.synthmet.2010.04.021.

(4) Choi, S.; Lee, H.; Ghaffari, R.; Hyeon, T.; Kim, D. H. Recent Advances in Flexible and Stretchable Bio-Electronic Devices Integrated with Nanomaterials. *Adv. Mater.* **2016**, *28* (22), 4203–4218. https://doi.org/10.1002/adma.201504150.

(5) Zhang, P.; Wang, F.; Yu, M.; Zhuang, X.; Feng, X. Two-Dimensional Materials for Miniaturized Energy Storage Devices: From Individual Devices to Smart Integrated Systems. *Chem. Soc. Rev.* **2018**, *47* (19), 7426–7451. https://doi.org/10.1039/c8cs00561c.

(6) Chen, H.; Xu, Y.; Zhang, J.; Wu, W.; Song, G. Enhanced Stretchable Graphene-Based Triboelectric Nanogenerator via Control of Surface Nanostructure. *Nano Energy* **2019**, *58* (December 2018), 304–311. https://doi.org/10.1016/j.nanoen.2019.01.029.

(7) Li, Z.; Hu, K.; Li, Z.; Li, C.; Deng, Y. Polypyrrole-Stabilized Polypeptide for Eco-Friendly Supercapacitors. *Int. J. Mol. Sci.* **2023**, *24* (3), 1–11. https://doi.org/10.3390/ijms24032497.

(8) Zhou, H.; Liu, Y.; Ren, M.; Zhai, H. J. Mechanically Exfoliated Graphite Paper with Layered Microstructures for Enhancing Flexible Electrochemical Energy Storage. *Inorg. Chem. Front.* **2022**, *9* (9), 1920–1930. https://doi.org/10.1039/d1qi01601f.

(9) Liang, A.; Li, D.; Zhou, W.; Wu, Y.; Ye, G.; Wu, J.; Chang, Y.; Wang, R.; Xu, J.; Nie, G.; Hou, J.; Du, Y. Robust Flexible WS2/PEDOT:PSS Film for Use in High-Performance Miniature Supercapacitors. *J. Electroanal. Chem.* **2018**, *824,* 136–146. https://doi.org/10.1016/j.jelechem.2018.07.040.

(10) Tian, X.; Li, X.; Yang, T.; Wang, K.; Wang, H.; Song, Y.; Liu, Z.; Guo, Q.; Chen, C. Flexible Carbon Nanofiber Mats with Improved Graphitic Structure as Scaffolds for Efficient All-Solid-State Supercapacitor. *Electrochim. Acta* **2017**, *247,* 1060–1071. https://doi.org/10.1016/j.electacta.2017.07.103.

(11) Na, W.; Jun, J.; Park, J. W.; Lee, G.; Jang, J. Highly Porous Carbon Nanofibers Co-Doped with Fluorine and Nitrogen for Outstanding Supercapacitor Performance. *J. Mater. Chem. A* **2017**, *5* (33), 17379–17387. https://doi.org/10.1039/c7ta04406b.

(12) Yu, M. F.; Lourie, O.; Dyer, M. J.; Moloni, K.; Kelly, T. F.; Ruoff, R. S. Strength and Breaking Mechanism of Multiwalled Carbon Nanotubes under Tensile Load. *Science (80-.).* **2000**, *287* (5453), 637–640. https://doi.org/10.1126/science.287.5453.637.

(13) Iakunkov, A.; Skrypnychuk, V.; Nordenström, A.; Shilayeva, E. A.; Korobov, M.; Prodana, M.; Enachescu, M.; Larsson, S. H.; Vtalyzin, A. Activated Graphene as a Material for Supercapacitor Electrodes: Effects of Surface Area, Pore Size Distribution and Hydrophilicity. *Phys. Chem. Chem. Phys.* **2019**, *21* (32), 17901–17912.

https://doi.org/10.1039/c9cp03327k.

(14) Sun, C. Bin; Zhong, Y. W.; Fu, W. J.; Zhao, Z. Q.; Liu, J.; Ding, J.; Han, X. P.; Deng, Y. Da; Hu, W. Bin; Zhong, C. Tungsten Disulfide-Based Nanomaterials for Energy Conversion and Storage. *Tungsten* **2020**, *2* (2), 109–133. https://doi.org/10.1007/s42864-020-00038-6.

(15) Liu, S.; Zeng, Y.; Zhang, M.; Xie, S.; Tong, Y.; Cheng, F.; Lu, X. Binder-Free WS2 Nanosheets with Enhanced Crystallinity as a Stable Negative Electrode for Flexible Asymmetric Supercapacitors. *J. Mater. Chem. A* **2017**, *5* (40), 21460–21466. https://doi.org/10.1039/c7ta07009h.

(16) Lyu, L.; Hooch Antink, W.; Kim, Y. S.; Kim, C. W.; Hyeon, T.; Piao, Y. Recent Development of Flexible and Stretchable Supercapacitors Using Transition Metal Compounds as Electrode Materials. *Small* **2021**, *17* (36), 1–41. https://doi.org/10.1002/smll.202101974.

(17) Yun, Q.; Lu, Q.; Zhang, X.; Tan, C.; Zhang, H. Three-Dimensional Architectures Constructed from Transition-Metal Dichalcogenide Nanomaterials for Electrochemical Energy Storage and Conversion. *Angew. Chemie - Int. Ed.* **2018**, *57* (3), 626–646. https://doi.org/10.1002/anie.201706426.

(18) Zeng, H.; Liu, G. Bin; Dai, J.; Yan, Y.; Zhu, B.; He, R.; Xie, L.; Xu, S.; Chen, X.; Yao, W.; Cui, X. Optical Signature of Symmetry Variations and Spin-Valley Coupling in Atomically Thin Tungsten Dichalcogenides. *Sci. Rep.* **2013**, *3*, 2–6. https://doi.org/10.1038/srep01608.

(19) Yang, X.; Li, J.; Hou, C.; Zhang, Q.; Li, Y.; Wang, H. Skeleton-Structure WS2@CNT Thin-Film Hybrid Electrodes for High-Performance Quasi-Solid-State Flexible Supercapacitors. *Front. Chem.* **2020**, *8* (June), 1–10. https://doi.org/10.3389/fchem.2020.00442.

(20) Zhang, D.; Wang, H.; Cheng, J.; Han, C.; Yang, X.; Xu, J.; Shan, G.; Zheng, G.; Cao, M. Conductive WS2-NS/CNTs Hybrids Based 3D Ultra-Thin Mesh Electromagnetic Wave Absorbers with Excellent Absorption Performance. *Appl. Surf. Sci.* **2020**, 147052. https://doi.org/10.1016/j.apsusc.2020.147052.

(21) Boll, F.; Crisci, M.; Merola, L.; Lamberti, F.; Smarsly, B.; Gatti, T. Assessing the Effect of Stabilization and Carbonization Temperatures on Electrochemical Performance of Electrospun Carbon Nanofibers from Polyacrylonitrile. *Adv. Energy Sustain. Res.* **2023**, *4* (11), 2300121. https://doi.org/10.1002/aesr.202300121.

(22) Tan, Y.; Lin, D.; Liu, C.; Wang, W.; Kang, L.; Ran, F. Carbon Nanofibers Prepared by Electrospinning Accompanied with Phase-Separation Method for Supercapacitors: Effect of Thermal Treatment Temperature. *J. Mater. Res.* **2018**, *33* (9), 1120–1130. https://doi.org/10.1557/jmr.2017.373.

(23) Biccai, S.; Barwich, S.; Boland, D.; Harvey, A.; Hanlon, D.; McEvoy, N.; Coleman, J. N. Exfoliation of 2D Materials by High Shear Mixing. *2D Mater.* **2019**, *6* (1), 015008. https://doi.org/10.1088/2053-1583/aae7e3.

(24) Coleman, J. N.; Lotya, M.; O'Neill, A.; Bergin, S. D.; King, P. J.; Khan, U.; Young, K.; Gaucher, A.; De, S.; Smith, R. J.; Shvets, I. V.; Arora, S. K.; Stanton, G.; Kim, H. Y.; Lee, K.; Kim, G. T.; Duesberg, G. S.; Hallam, T.; Boland, J. J.; Wang, J. J.; Donegan, J. F.; Grunlan, J. C.; Moriarty, G.; Shmeliov, A.; Nicholls, R. J.; Perkins, J. M.; Grieveson,

E. M.; Theuwissen, K.; McComb, D. W.; Nellist, P. D.; Nicolosi, V. Two-Dimensional Nanosheets Produced by Liquid Exfoliation of Layered Materials. *Science (80-.).* **2011**, *331* (6017), 568–571. https://doi.org/10.1126/science.1194975.

(25) Backes, C.; Campi, D.; Szydlowska, B. M.; Synnatschke, K.; Ojala, E.; Rashvand, F.; Harvey, A.; Griffin, A.; Sofer, Z.; Marzari, N.; Coleman, J. N.; O'Regan, D. D. Equipartition of Energy Defines the Size-Thickness Relationship in Liquid-Exfoliated Nanosheets. *ACS Nano* **2019**, 13, 7050–7061. https://doi.org/10.1021/acsnano.9b02234.

(26) Griffin, A.; Nisi, K.; Pepper, J.; Harvey, A.; Szydłowska, B. M.; Coleman, J. N.; Backes, C. Effect of Surfactant Choice and Concentration on the Dimensions and Yield of Liquid-Phase-Exfoliated Nanosheets. *Chem. Mater.* **2020**, *32* (7), 2852–2862. https://doi.org/10.1021/acs.chemmater.9b04684.

(27) Deitzel, J. M.; Kleinmeyer, J. D.; Hirvonen, J. K.; Beck Tan, N. C. Controlled Deposition of Electrospun Poly(Ethylene Oxide) Fibers. *Polymer (Guildf).* **2001**, *42* (19), 8163–8170. https://doi.org/10.1016/S0032-3861(01)00336-6.

(28) Cárdenas-Martínez, J.; España-Sánchez, B. L.; Esparza, R.; Ávila-Niño, J. A. Flexibleand Transparent Supercapacitors Using Electrospun PEDOT:PSS Electrodes. *Synth. Met.* **2020**, *267* (March), 116436. https://doi.org/10.1016/j.synthmet.2020.116436.

(29) Schmitz, F.; Lago, N.; Fagiolari, L.; Burkhart, J.; Cester, A.; Polo, A.; Prato, M.; Meneghesso, G.; Gross, S.; Bella, F.; Lamberti, F.; Gatti, T. High Open-Circuit Voltage Cs2AgBiBr6 Carbon-Based Perovskite Solar Cells via Green Processing of Ultrasonic Spray-Coated Carbon Electrodes from Waste Tire Sources. *ChemSusChem* **2022**, *15* (22). https://doi.org/10.1002/cssc.202201590.

(30) O'Connor, I.; De, S.; Coleman, J. N.; Gun'ko, Y. K. Development of Transparent, Conducting Composites by Surface Infiltration of Nanotubes into Commercial Polymer Films. *Carbon N. Y.* **2009**, *47* (8), 1983–1988. https://doi.org/10.1016/j.carbon.2009.03.048.

(31) McCullen, S. D.; Stevens, D. R.; Roberts, W. A.; Ojha, S. S.; Clarke, L. I.; Gorga, R. E. Morphological, Electrical, and Mechanical Characterization of Electrospun Nanofiber Mats Containing Multiwalled Carbon Nanotubes. *Macromolecules* **2007**, *40* (4), 997–1003. https://doi.org/10.1021/ma061735c.

(32) Bauhofer, W.; Kovacs, J. Z. A Review and Analysis of Electrical Percolation in Carbon Nanotube Polymer Composites. *Compos. Sci. Technol.* **2009**, *69* (10), 1486–1498. https://doi.org/10.1016/j.compscitech.2008.06.018.

(33) Rashid, T. U.; Gorga, R. E.; Krause, W. E. Mechanical Properties of Electrospun Fibers—A Critical Review. *Adv. Eng. Mater.* **2021**, *23* (9), 1–26. https://doi.org/10.1002/adem.202100153.

(34) Crisci, M.; Boll, F.; Merola, L.; Pflug, J. J.; Liu, Z.; Gallego, J.; Lamberti, F.; Gatti, T. Nanostructured 2D WS2@PANI Nanohybrids for Electrochemical Energy Storage. *Front. Chem.* **2022**, *10* (September), 1–11. https://doi.org/10.3389/fchem.2022.1000910.

(35) Delabie, A.; Caymax, M.; Groven, B.; Heyne, M.; Haesevoets, K.; Meersschaut, J.; Nuytten, T.; Bender, H.; Conard, T.; Verdonck, P.; Van Elshocht, S.; De Gendt, S.; Heyns, M.; Barla, K.; Radu, I.; Thean, A. Low Temperature Deposition of 2D WS2 Layers from WF6 and H2S Precursors: Impact of Reducing Agents. *Chem. Commun.* **2015**, *51* (86), 15692–15695. https://doi.org/10.1039/c5cc05272f.

(36) Sun, G.; Zhou, J.; Yu, F.; Zhang, Y.; Pang, J. H. L.; Zheng, L. Electrochemical Capacitive Properties of CNT Fibers Spun from Vertically Aligned CNT Arrays. *J. Solid State Electrochem.* **2012**, *16* (5), 1775–1780. https://doi.org/10.1007/s10008-011-1606-2.

(37) Kriegel, I.; Ghini, M.; Bellani, S.; Zhang, K.; Jansons, A. W.; Crockett, B. M.; Koskela, K. M.; Barnard, E. S.; Penzo, E.; Hutchison, J. E.; Robinson, J. A.; Manna, L.; Borys, N. J.; Schuck, P. J. Light-Driven Permanent Charge Separation across a Hybrid Zero-Dimensional/Two-Dimensional Interface. *J. Phys. Chem. C* **2020**, *124* (14), 8000–8007. https://doi.org/10.1021/acs.jpcc.0c01147.

(38) Torad, N. L.; Salunkhe, R. R.; Li, Y.; Hamoudi, H.; Imura, M.; Sakka, Y.; Hu, C. C.; Yamauchi, Y. Electric Double-Layer Capacitors Based on Highly Graphitized Nanoporous Carbons Derived from ZIF-67. *Chem. - A Eur. J.* **2014**, *20* (26), 7895–7900. https://doi.org/10.1002/chem.201400089.

(39) Gogotsi, Y.; Penner, R. M. Energy Storage in Nanomaterials - Capacitive, Pseudocapacitive, or Battery-Like? *ACS Nano* **2018**, *12* (3), 2081–2083. https://doi.org/10.1021/acsnano.8b01914.

(40) Lukatskaya, M. R.; Dunn, B.; Gogotsi, Y. Multidimensional Materials and Device Architectures for Future Hybrid Energy Storage. *Nat. Commun.* **2016**, *7*. https://doi.org/10.1038/ncomms12647.

(41) Kuc, A.; Zibouche, N.; Heine, T. Influence of Quantum Confinement on the Electronic Structure of the Transition Metal Sulfide TS2. *Phys. Rev. B - Condens. Matter Mater. Phys.* **2011**, *83* (24), 1–4. https://doi.org/10.1103/PhysRevB.83.245213.

(42) Splendiani, A.; Sun, L.; Zhang, Y.; Li, T.; Kim, J.; Chim, C. Y.; Galli, G.; Wang, F. Emerging Photoluminescence in Monolayer MoS2. *Nano Lett.* **2010**, *10* (4), 1271–1275. https://doi.org/10.1021/nl903868w.

(43) Berkdemir, A.; Gutiérrez, H. R.; Botello-Méndez, A. R.; Perea-López, N.; Elías, A. L.; Chia, C. I.; Wang, B.; Crespi, V. H.; López-Urías, F.; Charlier, J. C.; Terrones, H.; Terrones, M. Identification of Individual and Few Layers of WS2 Using Raman Spectroscopy. *Sci. Rep.* **2013**, *3*, 1–8. https://doi.org/10.1038/srep01755.

(44) Abdelkader, A. M.; Kinloch, I. A. Mechanochemical Exfoliation of 2D Crystals in Deep Eutectic Solvents. *ACS Sustain. Chem. Eng.* **2016**, *4* (8), 4465–4472. https://doi.org/10.1021/acssuschemeng.6b01195.

(45) Sourisseau, C.; Cruege, F.; Fouassier, M.; Alba, M. Second-Order Raman Effects, Inelastic Neutron Scattering and Lattice Dynamics in 2H-WS2. *Chem. Phys.* **1991**, *150* (2), 281–293. https://doi.org/10.1016/0301-0104(91)80136-6.

(46) Gutiérrez, H. R.; Perea-López, N.; Elías, A. L.; Berkdemir, A.; Wang, B.; Lv, R.; López-Urías, F.; Crespi, V. H.; Terrones, H.; Terrones, M. Extraordinary Room-Temperature Photoluminescence in Triangular WS 2 Monolayers. *Nano Lett.* **2013**, *13* (8), 3447–3454. https://doi.org/10.1021/nl3026357.

(47) Zhang, H. Bin; Lin, G. D.; Zhou, Z. H.; Dong, X.; Chen, T. Raman Spectra of MWCNTs and MWCNT-Based H2-Adsorbing System. *Carbon N. Y.* **2002**, *40* (13), 2429–2436. https://doi.org/10.1016/S0008-6223(02)00148-3.

(48) Eklund, P. C.; Holden, J. M.; Jishi, R. A. Vibrational Modes of Carbon Nanotubes; Spectroscopy and Theory. *Carbon N. Y.* **1995**, *33* (7), 959–972. https://doi.org/10.1016/0008-6223(95)00035-C.

(49) Dresselhaus, M. S.; Dresselhaus, G.; Saito, R.; Jorio, A. Raman Spectroscopy of Carbon Nanotubes. *Phys. Rep.* **2005**, *409* (2), 47–99. https://doi.org/10.1016/j.physrep.2004.10.006.

(50) Langford, J. I.; Wilson, A. J. . C. Scherrer after Sixty Years: A Survey and Some New Results in the Determination of Crystallite Size. *J. Appl. Cryst. (1978).* **1977**, *11*, 102–113.

(51) Monshi, A.; Foroughi, M. R.; Monshi, M. R. Modified Scherrer Equation to Estimate More Accurately Nano-Crystallite Size Using XRD. *World J. Nano Sci. Eng.* **2012**, *02* (03), 154–160. https://doi.org/10.4236/wjnse.2012.23020.

(52) Gharbi, O.; Tran, M. T. T.; Tribollet, B.; Turmine, M.; Vivier, V. Revisiting Cyclic Voltammetry and Electrochemical Impedance Spectroscopy Analysis for Capacitance Measurements. *Electrochim. Acta* **2020**, *343*, 136109. https://doi.org/10.1016/j.electacta.2020.136109.

(53) Simotwo, S. K.; Delre, C.; Kalra, V. Supercapacitor Electrodes Based on High-Purity Electrospun Polyaniline and Polyaniline-Carbon Nanotube Nanofibers. *ACS Appl. Mater. Interfaces* **2016**, *8* (33), 21261–21269. https://doi.org/10.1021/acsami.6b03463.

(54) Rountree, K. J.; Mccarthy, B. D.; Rountree, E. S.; Eisenhart, T. T.; Dempsey, J. L. A Practical Beginner ' s Guide to Cyclic Voltammetry. *J. Chem. Educ.* **2017**. https://doi.org/10.1021/acs.jchemed.7b00361.

(55) Kumar, P.; Vasita, R. Understanding the Relation between Structural and Mechanical Properties of Electrospun Fiber Mesh through Uniaxial Tensile Testing. *J. Appl. Polym. Sci.* **2017**, *134* (26), 45012. https://doi.org/10.1002/app.45012.

(56) Wenelska, K.; Maślana, K.; Mijowska, E. Study on the Flammability, Thermal Stability and Diffusivity of Polyethylene Nanocomposites Containing Few Layered Tungsten Disulfide (WS2) Functionalized with Metal Oxides. *RSC Adv.* **2018**, *8* (23), 12999–13007. https://doi.org/10.1039/c8ra01527a.

(57) Portet, C.; Yushin, G.; Gogotsi, Y. Electrochemical Performance of Carbon Onions, Nanodiamonds, Carbon Black and Multiwalled Nanotubes in Electrical Double Layer Capacitors. *Carbon N. Y.* **2007**, *45* (13), 2511–2518. https://doi.org/10.1016/j.carbon.2007.08.024.

(58) Alcántara, R.; Jiménez-Mateos, J. M.; Lavela, P.; Tirado, J. L. Carbon Black: A Promising Electrode Material for Sodium-Ion Batteries. *Electrochem. commun.* **2001**, *3* (11), 639–642. https://doi.org/10.1016/S1388-2481(01)00244-2.

(59) Fransson, L.; Eriksson, T.; Edström, K.; Gustafsson, T.; Thomas, J. O. Influence of Carbon Black and Binder on Li-Ion Batteries. *J. Power Sources* **2001**, *101* (1), 1–9. https://doi.org/10.1016/S0378-7753(01)00481-5.

(60) Shao, M.; Ning, F.; Zhao, Y.; Zhao, J.; Wei, M.; Evans, D. G.; Duan, X. Core-Shell Layered Double Hydroxide Microspheres with Tunable Interior Architecture for Supercapacitors. *Chem. Mater.* **2012**, *24* (6), 1192–1197. https://doi.org/10.1021/cm203831p.

(61) Gao, Z.; Wang, J.; Li, Z.; Yang, W.; Wang, B.; Hou, M.; He, Y.; Liu, Q.; Mann, T.; Yang, P.; Zhang, M.; Liu, L. Graphene Nanosheet/Ni2+/Al3+ Layered Double-Hydroxide Composite as a Novel Electrode for a Supercapacitor. *Chem. Mater.* **2011**, *23* (15), 3509–3516. https://doi.org/10.1021/cm200975x.

(62) Zhou, L.; Xing, L.; Zheng, Y.; Lai, X.; Su, J.; Deng, C.; Sun, T. A Study of External Surface Pressure Effects on the Properties for Lithium-Ion Pouch Cells. *Int. J. Energy Res.* **2020**, *44* (8), 6778–6791. https://doi.org/10.1002/er.5415.

(63) Lamberti, A.; Perrucci, F.; Caprioli, M.; Serrapede, M.; Fontana, M.; Bianco, S.; Ferrero, S.; Tresso, E. New Insights on Laser-Induced Graphene Electrodes for Flexible Supercapacitors: Tunable Morphology and Physical Properties. *Nanotechnology* **2017**, *28* (17), 174002. https://doi.org/10.1088/1361-6528/aa6615.

(64) Sun, G.; Zhang, X.; Lin, R.; Yang, J.; Zhang, H.; Chen, P. Hybrid Fibers Made of Molybdenum Disulfide, Reduced Graphene Oxide, and Multi-Walled Carbon Nanotubes for Solid-State, Flexible, Asymmetric Supercapacitors. *Angew. Chemie - Int. Ed.* **2015**, *54* (15), 4651–4656. https://doi.org/10.1002/anie.201411533.

Table of content

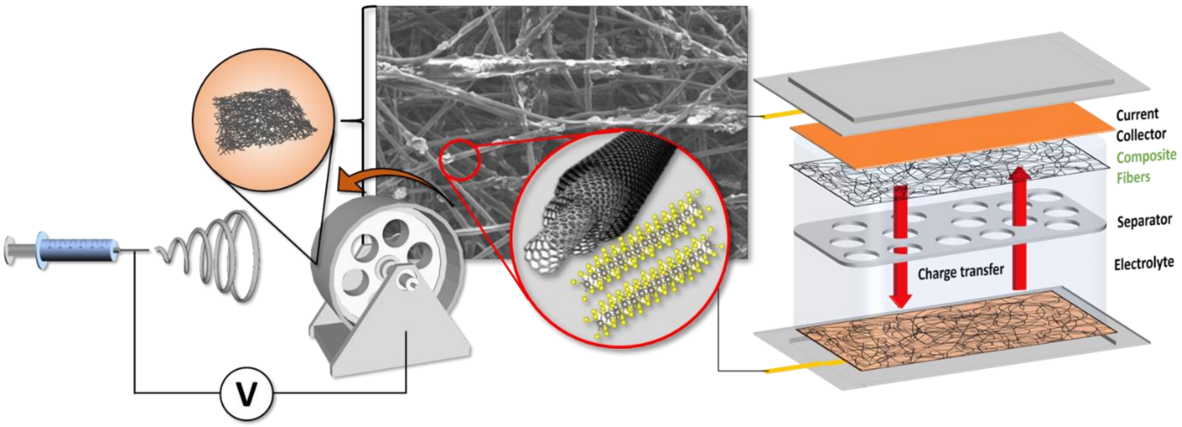

The authors confirm that all figures in the manuscript, the supporting information, as well as the TOC graphic, were taken and created solely by Felix Boll and have never been published previously in any journal or report.